12-20-2016

Dependence of Photoelectrochemical Properties on Geometry Factors of Interconnected “Caterpillar-like” ZnO Networks

Qiang Li
The University of Texas Rio Grande Valley

Xing Sun
The University of Texas Rio Grande Valley

Karen Lozano
The University of Texas Rio Grande Valley, karen.lozano@utrgv.edu

Yuanbing Mao

Recommended Citation

Li, Qiang, Xing Sun, Karen Lozano, and Yuanbing Mao. "Dependence of photoelectrochemical properties on geometry factors of interconnected “Caterpillar-like” ZnO networks." Electrochimica Acta 222 (2016): 232-245. https://doi.org/10.1016/j.electacta.2016.10.162

Version of Record: https://www.sciencedirect.com/science/article/pii/S0013468616322654
Manuscript_0064bf76da5d1c9571936a8b3eeb84c8

Dependence of Photoelectrochemical Properties on Geometry Factors of Interconnected "Caterpillar-like" ZnO Networks

Qiang Li[1,2,3], Xing Sun[1,3], Karen Lozano[2], and Yuanbing Mao[1,*]
[1]Department of Chemistry, University of Texas Rio Grande Valley, 1201 West University Drive, Edinburg, TX 78539 USA
[2]Department of Mechanical Engineering, University of Texas Rio Grande Valley, Edinburg, TX 78539 USA
[3]Current address: Department of Materials Science & Engineering, Texas A&M University, College Station, TX 77843 USA
[*]Author to whom correspondence should be addressed: Tel: +1 956 665 2417; Fax: +1 956 665 5006; E-mail: yuanbing.mao@utrgv.edu

Abstract

To elevate the spatial occupancy of one-dimensional ZnO nanostructures and overcome the limitations of multistep seeding methods currently widely used, a rational, facile and high-yielding procedure has been reported by our group previously for the fabrication of the interconnected three-dimensional "caterpillar-like" ZnO nanostructured networks (CZNs) for photoelectrochemical applications. In this work, by fine-tuning the synthesis procedure and manipulating the growth process of the ZnO nanostructures, we investigated the dependence of their photoelectrochemical properties on geometry factors of these unique CZNs consisting of branched ZnO nanowires onto ZnO nanofibers with improved and tunable surface-to-volume ratio and roughness factor. They offer mechanically and electrically robust interconnected networks with open micrometer-scale structures and short hole diffusion length. We further studied the preferential light-material interaction and charge separation to maximize the photo-to-hydrogen conversion efficiency. When used as photoanode, our CZNs not only favor sunlight harvesting with multireflection ability, but also suppress the recombination of photogenerated charge. Compared to the literature results, our CZN photoanodes with ZnO nanobranches of ~2.2 μm in length and ~25 nm in diameter exhibited the highest photocurrent density of 0.72 $mA \cdot cm^{-2}$ at +1.2 V (versus Ag/AgCl) and conversion efficiency of 0.209% at +0.91 V (versus RHE) without decorating with noble metal cocatalysts or nonmetallic/metallic doping due to their favorable structural features. Overall, our procedure to obtain the desirable CZN fetches in opportunities for facile and efficient fabrication of model photoelectrochemical anodes and would be applied to other materials for sustainable chemistry and engineering applications.

Highlights

Hierarchical “caterpillar-like” ZnO nanostructures have been prepared through a hybrid route.

The ease and high throughput of the method favors a feasible PEC applications.

The tunability of the geometric factors could optimize the light-material interaction.

Ultralong and ultrathin branches shorten minority carrier diffusion lengths to further improve PEC performance.

Keywords

ZnO; Nanostructured networks; Photoanodes; Light-material interaction; Diffusion lengths.

1. Introduction

The recent surge of alternative clean energy with minimal environmental impact in a cost-effective way requires the exploration of new materials and/or structures as efficient electrodes for industry-level photoelectrochemical (PEC) water splitting into usable H_2 fuel [1-5]. Since Honda and Fujishima reported electrochemical photolysis at the TiO_2/liquid junction [6], considerable efforts have been made on anodic/cathodic photoelectrolysis of water with metal oxides, which have been featured by their abundance, environmental friendliness, and chemical stability [7,8]. With a wide direct band gap (3.37 eV at 300 K) and a large exciton binding energy (60 meV), n-type ZnO has been studied as a promising photoanode material at various realms like photocatalysis and photovoltaics [9,10]. It has an electron mobility 2-3 orders of magnitude higher than TiO_2 to efficiently suppress charge recombination [11]. In addition, it can be easily crystallized and induced into anisotropic structures as high performance photoanode with potentially high solar-to-hydrogen conversion efficiency [12,13].

Nowadays it is well-known that nanomaterials could outperform their bulk counterparts in many aspects because of increased interacting sites, shorter lateral diffusion distance and lower reflectivity [14]. Assembling nano-building blocks into desirable structures is a further advanced intelligent tactic for realizing higher performance and better functionality by exploiting new hierarchy and scaling-up laws [15-17]. For example, even with high surface-to-volume ratio, photoanodes composed of 15-40 nm nanoparticles (NPs) delivered a photocurrent density at the highest of only 0.142 mA cm^{-2} (at 1.0 V *vs* Ag/AgCl) since NPs suffer from a serious charge recombination at surface defects and grain boundaries [18]. In contrast, monocrystalline ZnO nanowires/nanorods and their arrays provide a direct conducting passageway for rapid collection of photoexcited electrons from injection spot to back contact, but their inadequate surface area and low absorbed photo flux gave poor photocurrent value ($\leq$ 0.115 mA·cm^{-2} at 1.21 V *vs* RHE) [19-23]. To meet the challenges, hierarchical 3-D nanostructures integrating 1-D conduction trunks and secondary branches, e.g. dendritic nanowires (NWs)/nanofibers (NFs), are particularly desired in light of the greatly improved light-harvesting, the efficient charge separation and short hole diffusion length (L_D) for which the refined secondary structures are

responsible [24-27]. One consensus that favored 3-D nanoarchitectures are evidently superior to 0-D and 1-D counterparts has been reached in dye-sensitized solar cells (DSSCs) and microsupercapacitors using 3-D ZnO nanoforests. Specifically, Ko et al. reported that the overall light-conversion efficiency (2.63%) of the branched ZnO "nanotree" DSSCs was 5 times higher than the efficiency of upstanding NWs through a multiple seeding approach using all solution processed hydrothermal method.[12] We reported that 3-D ZnO nanoforests used as framework to carry pseudocapacitive materials exhibited 5 times higher areal capacitance than the corresponding nanowire arrays [28]. In PEC water splitting, 3-D morphologically created ZnO nanostructures capable of greatly boosting the solar-to-hydrogen conversion efficiency lacks successful examples and insufficient relevant approaches have been carried out except that branched nanotetrapods were successfully synthesized recently via oxidative metal vapor transport deposition, and its corresponding undoped photoanode delivered a photocurrent density of 0.12 $mA \cdot cm^{-2}$ at 0.92 V versus RHE [29]. The low branch density and the blocked light path into deep cavities owing to the compact stack of nanotetrapods supposedly limited the electrode performances. To fill this void, our group adopted seeding method to fine tailor the 3-D branched ZnO nanotrees, wherein the superior architectural qualities, such as highly augmented surface-to-volume ratio and shortened lateral hole diffusion length, endow willow-like ZnO nanoforest with a highest photocurrent density of 0.919 $mA \cdot cm^{-2}$ at 1.2 V versus Ag/AgCl [30].

However, in terms of methodology, the seeding method in solution phase still confronts some engineering obstacles notwithstanding it being regarded as a major avenue to fabricate heterogeneous nanostructures of semiconductors [12,16,30-32]. Typically, the fabrication method of a 3-D upstanding nanoforest can be encapsulated as follow: as-prepared colloidal quantum dots as seeds are spin-coated or drop-casted onto substrates to grow length-wise NWs hydrothermally and reduplicate seeding steps need to be conducted for subordinate NW growth on trunks to obtain multigeneration nanostructures. The seeding method is a cost-effective procedure with low synthesis temperature and ease of scaling up, which account for its prevalence, in remarkable comparison with expensive and complex factor-dependent vapor-liquid-solid (VLS), metal-organic chemical vapor deposition (MOCVD) and magnetron sputtering methods which need either extreme requisites like high temperatures or the assistance of noble metal catalysts [19,21,33-36]. However, the seeding method still holds the following drawbacks. First, the uneven coverage of subordinate NWs on the trunks impedes optimum light

absorption and electron transport to some extent. Second, excessive seeds are bound to aggregate on the near surface of the back contact, thereby increasing the chance of charge recombination and blocking the light path. Thirdly, colloidal quantum dot preparation, multistep seeding processes and repeated capping agent removal by annealing lead to production complication, which contradicts the ease of manufacturing. Moreover, in the fabrications of upstanding branched nanostructures, the inadequate utilization of spare space among individual nanowires reduces surface-to-volume ratio and conversion efficiency. Therefore, an innovative protocol to generate 3-D nanostructures that is simple, effective and high-yielding will be appreciated for efficient PEC water splitting and other energy conversion/storage applications.

Recently, we reported a novel "caterpillar-like" ZnO nanoarchitecture (CZN) with high spatial occupancy of NWs in an effort to substitute the well-accepted multistep seeding method.[37] The 3-D disposal of seeds has been actualized by piling polycrystalline seed-assembled nanofibers (NFs), deriving from annealing the polyvinylpyrrolidone (PVP)/$Zn(NO_3)_2$ precursor fibers produced by the Forcespinning (FS) technology, onto a substrate. Secondary NWs as branches would laterally burgeon from these polycrystalline seed-assembled NFs in a 360° fashion along their axial direction (c-axis) in a hydrothermal reaction to give an electrically and mechanically interconnected robust network. A sketch of fabricating typical 3-D "caterpillar-like" ZnO network is illustrated in **Scheme 1**. The CZN photoanodes of ~10 μm thick delivered a maximum photocurrent density of 0.524 $mA \cdot cm^{-2}$ at 1.2 V (*vs* Ag/AgCl), about 51% higher than that of the upstanding ZnO NW arrays. However, a fine structural control has not been done for a promoted PEC performance. A continuous and systematic study aiming at morphology-wise fine-tuning the "caterpillar-like" ZnO structures in order to optimize the light-material interactions and charge separation seeking a maximum solar-to-hydrogen conversion efficiency is presented here by exploring the versatility and cooperation of the reactants to control hydrolysis rate and ion saturation degree during the hydrothermal reaction. Not only was a facile and scalable synthesis of 3-D nanostructures dedicated to the PEC water splitting society, but also a synthesis-structure-property relation was studies for identifying optimum geometry with improved hole transfer length, electron transport pathways and light-harvesting capability. The optimized 3-D structures could serve a skeleton to carry noble metals, dopant and active coatings for a feasible practice of involving nanostructures in industrial production.

2. Experimental

2.1 Preparation of ZnO nanofibers and corresponding photoanodes:

The process of preparing PVP/$Zn(NO_3)_2$ fibers *via* Forcespinning was previously depicted in detail by our group [37]. Uniform composite fibers with ~800 nm in diameter were driven through equally circumferentially spaced orifices by rotating FS spinneret fed with viscous PVP/$Zn(NO_3)_2$ stock solution at 9000 rpm and then folded into 1 $inch^2$ mats after collected off the aluminum collectors. A production rate of ~0.68 g min^{-1} was determined. The ZnO NFs that comprise of ~10 nm ZnO nanocrystals were prepared by heating the as-spun PVP/$Zn(NO_3)_2$ fibrous mat to 500°C in air at a ramp rate of 2°C·min^{-1} and held isothermally for 3 h to remove the carrier polymer PVP.

To prepare corresponding photoanode, 2 g ZnO NFs in the powder form were homogeneously dispersed first in 10 mL of 1-butanol (≥ 99%, Sigma-Aldrich) by 5 min low energy sonication. Subsequently, an airbrush technique operated at a spray pressure of 10 psi was employed to deposit the suspension paste onto 180 nm indium tin oxide (ITO)-coated glass substrates (MTI Co., ≤ 15 Ω·$square^{-1}$) and the ZnO NF-carried ITO substrates were dried in vacuum oven at 80°C overnight and then heated at 350°C for 10 min to enhance the bond strength. This sample prior to branch growth was denoted, hereafter, as ZnO NFs. The deposition thickness of the ZnO NFs on ITO substrates was controlled to be ~8 μm by adjusting spray duration.

2.2 Preparation of caterpillar-like ZnO photoanodes:

The CZN were developed on the ZnO NF-carried ITO substrates by using the hydrothermal method reported previously with further optimization [12,28,30,37]. In a typical growth, a ZnO NF-carried ITO substrate was immersed in an aqueous nutrient solution containing 0.025 M zinc nitrate hexahydrate, 0.025 M hexamethylenetetramine ($C_6H_{12}N_4$, HMTA, ≥ 99%, Sigma-Aldrich), 0.0035 M polyethylenimine (PEI, M_w = ~800, Sigma-Aldrich), and 0-0.20 M ammonia ($NH_3·H_2O$, 28-30%, Sigma-Aldrich) at 95°C for 5 h to grow secondary ZnO branches originating from these ZnO NF seeds while the front side of the ITO substrate with active materials faced downward. The ammonia concentration was adjusted to tune the morphology of

the “caterpillar-like” ZnO nanostructures (CZN), which are prepared at three different ammonia concentrations of 0.10, 0.15 and 0.20 M, and are, hereafter, denoted as CZN-10, CZN-15 and CZN-20, respectively. These photoelectrodes after the ZnO branch growth were thoroughly rinsed with deionized water and ethanol, dried in a vacuum oven, and then annealed in air at 350°C for 10 min to remove the residual HMTA and PEI polymers.

2.3 Characterization:

A field-emission scanning electron microscopy (FESEM, Carl Zeiss Sigma VP, equipped with back-scatter electron detector) was used to examine the morphologies of the CZN specimens. The micrographs of transmission electron microscopy (TEM), high resolution TEM (HRTEM) and selected area electron diffraction (SAED) patterns were digitally recorded on a Hitachi H-9500 microscope with an accelerating voltage of 300 kV equipped with a SC-1000 Orius® TEM CCD Camera. The crystal structural information were determined using powder X-ray diffraction (XRD) (Bruker AXS D8 QUEST diffractometer with Cu Kα radiation (λ = 1.5406 Å)) and Raman spectroscopy (Bruker SENTERRA RAMAN microscope with a 785 nm laser as the excitation source). The surface textures and average roughness factors (R_a) of the CZN photoanodes were measured on a project area of 25 × 25 μm at a scanning frequency of 0.3 Hz using a VEECO Dimension 3000 atomic force microscope (AFM) and analyzed with the nanoscope analysis 1.5 software. The transmittance (T, %) and reflectance (R, %) of the various ZnO NF and CZN photoanodes were studied on a Lambda 950 UV-vis-NIR spectrophotometer and the absorption plus scattering ($A + S$, %) was deduced based on the formula $A + S = 100 – T – S$.

2.4 Photoelectrochemical (PEC) measurements:

PEC water splitting tests were performed in a standard three-electrode cell configuration, using the as-prepared ZnO NF or CZN photoanodes as the working electrode, a platinum wire as the counter electrode, Ag/AgCl in 1 M saturated KCl as the reference electrode and 0.5 M Na_2SO_4 solution buffered to pH ~7.0 with 0.1 M potassium phosphate buffer solution as the electrolyte purged with N_2 for 5–10 min before the PEC measurements take place. The J-V responses, electrochemical impedance spectroscopy (EIS) at 0.3 V DC mode at the frequency ranging of 0.01–1 MHz, and open circuit voltage decay (OCVD) were conducted on a Gamry reference 600

Potentiostat/Galvanostat/ZRA workstation under AM 1.5 G illumination projected from a solar simulator (1 sun, 100 $mV \cdot cm^{-2}$, Iwasaki Solar Simulation Evaluation Systems equipped with EYE/Iwasaki electronic ballast system and infrared filters). The light fixture was built with four metal halide-based arc lamps in the form of 2 × 2 array to ensure the light uniformity and the setup matches the solar spectrum within 5% error and is specified as IEC 60904-9 Class A standard (+/-2 %).

3. Results and discussions

3.1 Microstructural analysis and growth mechanism

As reported in our previous studies focusing on the fabrication, non-woven PVP/$Zn(NO_3)_2$ fibers with an average diameter of 800 nm were produced through FS process (**Scheme 1**). The simplistic and high-yielding FS technology takes advantage of strong centrifugal force to drive viscous precursor solutions through spinneret orifices for mass production of various fibers (~0.68 $g \cdot min^{-1}$ production rate for PVP/$Zn(NO_3)_2$ fibers), which meets the demands of mass manufacturing and plays a vital role in space-confining the size of ZnO nanoparticles in sub-15 nm range during the polymer carrier thermolysis as validated by our thermogram studies.[37] The FS technique was deliberately chosen over electrospinning because of its unique capability of driving highly viscous stock solution into fine fibers [38-40]. The heavy "polymer carrier" loading would invoke the nanoconfinement of ZnO nanocrystal growth in polymer skeleton during annealing [41]. The generated ultradense ZnO seeds with an average size of 10 nm in a fiber fashion eliminated the thermodynamic barriers and led to a deterministic heterogeneous growth of secondary ZnO NWs on the ZnO NFs [37]. The average diameter of ZnO NFs after polymer thermolysis shrunk to ~200 nm (**Scheme 1b**). High seed density of the ZnO NFs is a requisite for gaining highly dense secondary ZnO NWs as branches. As expected, highly dense secondary NWs whose density is estimated to be as high as ~1.6×10^{12} cm^{-2} have readily developed from their parental ZnO NFs hydrothermally. The NWs uniformly grew in a 360° fashion radially along the whole axial length, making the nanostructures rememble hairy caterpillars (**Scheme 1d**). A seris of time-dependent experiments were conducted to clarify the CZN-10 growth process for 5 h. After 1 h, the sprouts of ZnO nanostructures are apparent. Along

with extended time up to 5 h, subordinate NWs with increasing aspect ratio are gradually ripening (**Figure 1**).

To demonstrate the usage of these caterpillar nanostructures as photoanode materials, the airbrush spraying technique was adopted to deposit the ZnO fiber seeds onto ITO substrates up to ~8 μm in height by spraying the polycrystalline ZnO NFs-containing paste in 1-butanol prior to subordinate ZnO NW development. This method avoids the repeated high temperature treatments, *e.g.* 500°C, to the photoanodes for the polymer carrier removal and thus deteriorated electrical conductivity due to the segragation of ITO nanoparticles [42]. However, the moderate heat treatment at 350°C for 10 min to the photoanodes were found vital to enhance the bonding strength of the nanostructures to back contact and improve PEC performance before and after solution-processed subordinate NW growth on the parental ZnO NFs.

Densely distributed branches would multidimentionally sprout from the fiber seeds in due course to improve sunlight harvesting. One of the major findings in this work is to learn that the caterpillar nanostructures are morphology-programmable to optimize the light-material interactions and charge separation by manipulating the reaction agent cocentrations, especially ammonia. Three most promising nanostructures whose secondary branches have comparably high aspect ratios, *i.e.,* CZN-10, CZN-15 and CZn-20, were selected to be prepared to photoanodes for PEC applications. Besides displaying the morphology of the nanostructures, the topographic information of the actual photoanodes is very important to verify the quality control of active nanostructures on electrodes for reliable PEC studies. **Figure 2** shows the plan-view and cross-section SEM images of the typical PEC photoanodes of CZN-10, CZN-15 and CZn-20. As shown in high-magnication images as insets, the as-developed secondary NWs are polydirectionally arranged along the entire axial directions of the pristine ZnO NFs, allowing for a extremely high NW spatial occupancy, in remarkable contrast to vertically upstanding nanoforests with secondary NWs grown in a six-fold symmetry form fabricated via conventional seeding methods [12,28,30]. This configuration makes better use of void space in a give volume.[43] The hierarhical nanostructures remained intact after the secondary NW growth and have lengths of several tens of micrometers and are piled up layer-by-layer. The photoanodes possess open structures with micro-meter scale pores that facilitate the light penetration into

rooted regions and the light harvesting and scattering effects will be largely switched on due to the multireflection caused by the dense and polydirectional NWs. The caterpillar nanostructures wove into a mechanically and electrically robust networks because the secondary NWs with high length-to-diameter aspect ratios became interconnected. The associative long NWs construct the electron transportation paths as well as strengthen the physical and electrical contact between active materials and substrates. The different morphologies for three typical photoanodes are noticed. It is concluded that the ammonia concentration plays a very significant role in shaping the secondary ZnO NWs and it is noted that the length and the diameter of the branches increased and decreased, respectively, while the ammonia concentration exceeded 0.1 M and the $Zn(NO_3)_2 \cdot 6H_2O$/HMTA/PEI ratio was fixed at 1:1:0.14. Undoubtedly, the controllable structures are expected to deliver different optical properties and charge separation and transfer behaviors. The comprehension of reaction agents‘ influence in different crystall growth stages will be discussed in detail later.

The well-defined structures of the CZNs and the crystallographic growth directions of secondary NWs were further examined by performing transmission electron microscopy (TEM) on CZN-10 and CZn-20 (**Figure 3**). For both specimens, the fact that the secondary ZnO NWs stem from their parental ZnO NFs is validated. **Figures 3a&c and 3b&d** exhibit SEM and TEM images of an individual caterpillar of CZN-10 and CZN-20, respectively. The SAED patterns on **Figures 3c&d** indicate a polycrystalline feature, as indexed for the hexagonal wurtzite ZnO structure, for the individual caterpillars, which suggests the dense secondary ZnO NWs are aligned randomly on the pristine ZnO NFs [44]. The HRTEM images (**Figure 3e&f**) show that the secondary NWs are monocrystalline and highly crystallized with a lattice spacing of 0.26 nm between (0002) planes. Moreover, those secondary NWs grow along the [0001] direction. The single crystalline NWs as the building blocks, of which the caterpillars comprise, can greatly improve the charge carrier mobility and suppress the charge recombination. In a good agreement with the SEM studies, the length and diameter of the secondary NWs can be tuned by way of adjusting ammonia concentration. For instance, the NWs on CZN-20 are longer and ultrathin that the ones on CZN-10. The advantageous structure of CZN-20 is expected to better capture sunlight, facilitate charge transport and reduce hole diffusion distance for a further enhanced overall PEC performance [16,45]. X-ray diffraction (XRD) patterns were also performed on ZnO NFs and

CZNs (**Figure 4a**). Upon the structural evolution from the ZnO NFs to the CZNs, no obvious crystallographic preferred orientation was observed, probably due to the fact that the polydirectional ZnO NWs were rooted on the randomly oriented parental ZnO NFs unlike the vertically aligned ZnO NWs we reported previously [30]. Raman spectra were taken for further confirmation (**Figure 4b**). The most intensive mode in Raman spectra at ~439 cm^{-1} is assigned to E_2^{high}, corresponding to the oxygen sublattice vibration of wurtzite phase. Furthermore, the emergence of $E_2^{high} - E_2^{low}$ mode at ~333 cm^{-1} and $A_1(TO)$ mode at ~380 cm^{-1}, insensitive to (0001) facet, signifies the polydirectional growth of secondary NWs [46,47].

To clarify the geometry-property correlation, how the caterpillar structures evolve under the influence of reaction agents in precursor solutions, primarily ammonia, was studied. As widely stated in literature, the $Zn(NO_3)_2$ and HMTA that served as Zn^{2+} source and PH buffer by hydrolyzing and gradually releasing HCHO and NH_3, respectively, have commonly adopted for ZnO growth along its polar direction, *i.e.* [0001] [30,48,49]. From the inspection of the PEI effect on the secondary NW structures (data is not present here), it can be seen that only stubby rod-like secondary structures sprout from parental ZnO NFs in the precursor solution with no PEI and $NH_3 \cdot H_2O$ added. The PEI fosters the axial growth but constrain the lateral growth of the ZnO NWs by selectively adhering to the side surfaces as a capping agent. To study the $NH_3 \cdot H_2O$ effect on shaping structures, the ZnO NFs on the substrates were immersed in the nutrient solutions where the $Zn(NO_3)_2 \cdot 6H_2O$/HMTA/PEI ratio was fixed at 1:1:0.14 and $NH_3 \cdot H_2O$ concentration was changed from 0–0.2 M and a hydrothermal reaction at 95°C for 5 h was implemented afterwards for secondary NW development. It should be noted that various caterpillar ZnO nanostructures were reproduced on adhesive tapes adhered to titanium foils. On photoanode electrodes, the branched nanostructures are densely stacked and the secondary NWs nearly fully occupy inner space, as shown in **Figure 2**, so it has brought us trouble to concentrate on individual caterpillar-like ZnO hierarchical nanostructure and approach statistical analysis of their dimensions. Moreover, the scarcely distributed ZnO NFs on ITO substrates do not have strong associative connection, which caused debonding of ZnO NFs during secondary structure development. Therefore, we stuck less concentrated ZnO NFs to adhesive tapes and reproduced various caterpillar ZnO nanostructures distributed scarcely so that a single caterpillar-like ZnO nanostructure at different synthetic conditions can be clearly appreciated and statistically

analyzed, such as average length, diameter and density. As we observed in **Figure 5**, the structures of CZNs were strongly dependent on the $NH_3 \cdot H_2O$ concentration. CZNs with NW length and diameter of approximate 300 nm and 40 nm, respectively, were obtained with no $NH_3 \cdot H_2O$. After introducing 0.05 M $NH_3 \cdot H_2O$, the average length and diameter of CZNs was decreased to approximate 120 nm and 30 nm, respectively. However, using 0.10 M $NH_3 \cdot H_2O$ promoted the growth of secondary NWs whose average length and diameter was about 1.3 μm and 45 nm, respectivel, which suggests an obvious increments in dimensions. The length and diameter continued to increase to 1.95 μm and 50 nm, respectively, when adding 0.15 M $NH_3 \cdot H_2O$. Upon $NH_3 \cdot H_2O$ cencentration reaching 0.20 M, the average length of NWs achieved the highest value of about 2.2 μm in this study, whereas the NWs became ultrathin and the average diameter declined to 25 nm. When the $NH_3 \cdot H_2O$ cencentration was 0.25 M, the subordinate NWs were hardly seen and only wrecked NF stems remained. Furthermore, in sharp contrast to scarce NWs in the first two specimens, the pristine NF skeletons were compactly covered by dense secondary NWs just as $NH_3 \cdot H_2O$ concentrations was greater than 0.05 M but smaller than 0.25 M. Statistic analysis was done according to SEM studies (**Figure 5**) and the geometery factors, namely lengths and diameters, of secondary NWs are plotted versus $NH_3 \cdot H_2O$ concentrations in **Figure 5**. Three regions were illustrated in **Figure 5** so as to better interpret the distinct roles that the $NH_3 \cdot H_2O$ played. In region I ($[NH_3 \cdot H_2O] \leq 0.05$ M), low $NH_3 \cdot H_2O$ cencentration led to sparse and short ZnO branches due to that OH^- from ammonia hydrolysis scrambled for Zn^{2+} and produced unfavorable homogeneous nuclei, *i.e.* the $Zn(OH)_2$ precipitation; In region II, moderate $NH_3 \cdot H_2O$ concentrations ($0.5 \text{ M} < [NH_3 \cdot H_2O] \leq 0.15$ M) yielded dense, long and thicker NWs because sufficient $NH_3 \cdot H_2O$ could form $[Zn(NH_3)_4]^{2+}$ complexes which slowed down the release of Zn^{2+} for consecutive ZnO NW growth. In region III, when $[NH_3 \cdot H_2O]$ reached 0.20 M, the secondary was ~2.2 μm long and ~25 nm thin with the highest aspect ratio in this study, which displayed nano-needle morphology with sharp tips different from its hexagonal top surfaces of the other counterparts. We think that the extra ammonia provided an over-basic environment and the erosion from high $[NH_3 \cdot H_2O]$ to the secondary ZnO NWs is responsible for this unique needle-like structure. Specifically, the excessive $[NH_3 \cdot H_2O]$ could mediate the heterogeneous growth of ZnO NWs and simultaneously acuminate the shape of ZnO NWs through erosion. This was confirmed when the $[NH_3 \cdot H_2O]$ reached 0.25 M and no subordinate structures remained due to excessive $NH_3 \cdot H_2O$. This

phenomenon is in a great agreement with our study on vertically upstanding ZnO nanoforests.[30] Certain caterpillar nanostructures featured by ultradense, ultrathin and ultralong secondary NWs underlie the interest in promising use as active, doping matrix and/or supporting frameworks in PEC and other energy applications. The fine-tuned CZNs are expected to improve light-material interaction and charge transport and diffusion.

3.2 Optical properties

The optical characterizations of ZnO NFs and three exemplary CZNs, *i.e.* CZN-10, CZN-15 and CZN-20, were carried out using UV-Vis spectrophotometer to reveal the light absorption features along with structural evolution. The integrated light absorption plus scattering ($A + S$, %) was calculated by subtracting transmittance (T, %) and reflectance (R, %) from 100% incident light. Unlike those of the ZnO NFs, the transmittance spectra in **Figure 6a** and reflectance spectra in **Figure 6b** reveal that the optical properties of the three CZNs are very similar when the energy of excitation photons exceeds the ZnO band gap ($\lambda <$ ~388 nm), where these CZNs almost absorb all incident light while the other major difference is that the reflectance of the CZN-15 specimen is ~2% higher than its two CZN counterparts due to its unique physical features discussed below. The near/middle UV light's penetration depth of ~40 nm is within the dimensional scales of the branches of these CZNs, which endows the complete light absorption by these dense nanostructures.

The major variations of light transmittance and reflectance from these three CZNs occur within visible light region ($400 < \lambda < 800$ nm) and can be primarily attributed to the scattering event amongst primary and secondary ZnO nanostructures. The transmittance at $\lambda = 550$ nm through the CZN-10, CZN-15 and CZN-20 is 26.2, 12.6 and 16.4%, respectively (**Figure 6a**). The difference of T% among these three different nanostructures can arise from the difference of the ZnO NW lengths and diameters, and therefore, the surface coverage of the respective ZnO nanostructures on ITO substrates. This is in good agreement with our SEM studies (**Figures 2**). With the increase of $[NH_3 \cdot H_2O]$ in the range of 0.05-0.20 M, the CZN specimens accommodate dense ZnO NW branches with increasing lengths in the voids of the primary ZnO NF stems and thus significantly increases the volume filling factor of the CZNs. Furthermore, when the length

of the secondary ZnO NW branches increases to certain degree, the CZN forms an interconnected network decreasing the electrode transparency and light transmission. Meanwhile, the CZN-15 has thicker secondary NWs than the CZN-20 does, which reduced the transmittance due to higher coverage. The reflectance at λ = 550 nm from the CZN-10, CZN-15 and CZN-20 is 22.5, 18.6 and 20.3%, respectively (**Figure 6b**). This indicates more and more incident light is reflected among the dense secondary branches in a scattering mode along with evolving multi-dimensional complexity. As illustrated in **Figure 6d**, when it comes to the CZN-15 with very long but relative large branches, multiple reflection effect increases significantly, which eventually increases light absorption and lowers light surface reflection. The multiple reflections in the nanoforests extend the light absorption path and enable more interaction sites to associate with light [17,30]. The unique structural characteristics of CZN-15 result in the highest integrated light absorption plus scattering value ($A + S$, %) at λ = 550 nm of 68.7%, compared to 14.1% of ZnO NFs, 51.2% of CZN-10, and 63.2% of CZN-20 (**Figure 6c**). It should be noted that a portion of the ($A + S$, %) would derive from the 180 nm ITO nanoparticle coating on the glass substrates as well as the surface defect states of the ZnO nanostructures while this portion should be the same from these three samples since the same ITO substrate was used. Worth noting is that the CZN-15 captures and traps more incident light in comparison with ZnO NFs, CZN-10 and CZN-20, but the PEC studies discussed next proved the CZN-15 was not the champion architecture among typical photoanodes.

3.3 Surface roughness of photo anodes

To assist the optical characteristics of the ZnO NFs and CZNs, AFM measurements were carried out to reveal an important physical factor, *i.e.* the mean roughness factor (R_a). The R_a of the ZnO NFs and CZN-10, CZN-15 and CZN-20 measured on a project area of 25 × 25 μm was 761.1, 900.7, 1292 and 1207 nm, respectively (**Figure 7**). The R_a values are consistent with the optical results. It is worth noticing that the R_a of the pristine ZnO NFs is ~2.7 times higher than the 282.6 nm of the vertical ZnO NW array we reported [37]. The new 3-D disposal of fiber seeds could deliver a higher roughness than conventional vertically upstanding nanostructures. Overall, the increased volume filling factor by the multi-dimensional orientations of ZnO nanobranches plays an essential role to enhance light absorption through multiple light scattering. The precise

tailoring of morphology allows effective control of ZnO nanostructures over the UV-visible light absorption.

3.4 Photoelectrochemical properties

PEC measurements were carried out in a 0.5 m Na_2SO_4 electrolyte solutions buffered to pH value of 7.0 with phosphate buffer solutions using a three-electrode cell configuration. One key measurement is the photocurrent density versus potential (J-V) curves under the irradiation of AM 1.5 G simulated solar light (1 sun, 100 mW·cm^{-2}). **Figure 8a** shows a set of J-V curves with anodic linear sweep at 10 mV·s^{-1} from -0.5 to +1.2 V versus Ag/AgCl. When illuminated by standard solar light, the parental ZnO NFs produced a small photocurrent density of ~0.001 mA·cm^{-2} from -0.5 to +1.0 V and showed 0.089 mA·cm^{-2} at 1.2 V. In contrast to the parental NFs, the CZN-10 yielded a pronounced photocurrent density of 0.28 mA·cm^{-2} at +0.5 V and the density continued to increase to 0.41 mA·cm^{-2} at +1.2 V. The CZN-15 produced a further promoted photocurrent density of 0.38 mA·cm^{-2} at +0.5 V and 0.58 mA·cm^{-2} at +1.2 V. More impressively, the CZN-20 with ultralong and ultrathin branching NWs exhibited a more significant enhancement of photocurrent density of 0.44 mA·cm^{-2} at +0.5 V and 0.72 mA·cm^{-2} at +1.2 V, respectively. The dark linear scan sweep of ZnO NFs showed a negligible current in the range of 10^{-6} mA·cm^{-2}. It is seen that no saturation of photocurrent was observed in the J-V studies of these CZNs at positive potential region, implying efficient charge separation in these CZNs upon illumination. Meanwhile, we found out that post-heating treatment conducted at 350°C for 10 min to remove the residual polymer is critical to the high photocurrent delivery of caterpillar photoanodes and we think the residua would prevent the holes from splitting the water and thus result in significant charge recombination.

The photoelectrochemical efficiency (η) of all chosen photoanodes was evaluated *via* the equation:

$$\eta(photo)\% = \frac{100J_p}{I_0}(E^0_{rev} - |E_b|)$$

where j_p is the photocurrent density ($mA \cdot cm^{-2}$), E^0_{rev} is the standard state-reversible potential (1.23 V for water splitting), P_0 is the incident light intensity (100 $mW \cdot cm^{-2}$), and the E_b is the applied bias potential, which is the difference between the bias potential at which j_p is measured and the bias potential at the open circuit under the same illumination intensity. The potential measured against Ag/AgCl is converted to reversible hydrogen electrode (RHE) using the equation E(RHE) = E(Ag/AgCl) + 0.1976 V + 0.0059 pH. As shown in **Figure 8b**, the maximum efficiency for ZnO NF, CZN-10, CZN-15, and CZN-20 is 0.00066% (at 1.15 V versus RHE), 0.132% (at 0.84 V versus RHE), 0.187% (at 0.84 V versus RHE), and 0.209% (at 0.91 V versus RHE), respectively. Although the efficiency of CZN-10 is ~203 times higher than that of the pristine ZnO NFs, the efficiency of CZN-20 with the structural promotion continues to be improved ~58% higher than CZN-10 and ~42% higher than CZN-15.

In essence, to ascertain the enhanced PEC performances of the tunable CZNs, EIS was used for better insight into dynamics of interfacial charge transfer process. As presented in **Figure 8c**, the Nyquist plots regarding the three CZN photoelectrodes consist of a semicircle, whose diameter corresponds to the interface charge transfer resistance (R_{ct}) at the ZnO/electrolyte interface [50-53]. Besides the ZnO NFs, the CZN-20 comprising of branching ZnO NWs with high aspect ratio possess a smaller diameter of semicircle compared to CZN-10 and CZN-15 shows the smallest diameter of semicircle. After fitting the EIS data to the equivalent electrical circuit using the Randles-Ershler model, we found that the R_{ct} is 2134.3, 1398.1 and 1969.8 Ω for CZN-10, CZN-15 and CZN-20, respectively (**Table 1**). Our tentative answer to this phenomenon is that the elongated secondary branches for CZN-15 and CZN-20 construct better interconnected networks to motivate better charge transfer and the thicker NWs of CZN-15 with similar NW length compared to the ones of CZN-20 produce a further reduced charge transfer resistance.

In addition, the open circuit voltage decay technique was performed to clarify the bulk charge migration behavior in **Figure 8d**. When illuminated for the first 100 s, the open circuit voltage (V_{oc}) was observed to shift negatively with the increasing ZnO NW length. The secondary branches grown on the ZnO NFs build an interconnected network with high NW spatial occupancy and the steady-state charge carrier concentrations at the interconnected junction somehow decide the position of quasi-Fermi levels, which in turn determine the V_{oc}. Therefore,

the length of the secondary ZnO NWs is believed to be an important factor. The intimate association of secondary NWs of CZNs could reduce the bulk recombination. Conversely, under transient conditions when the illumination ceases, electrons and holes would facilely recombine at inner defects and boundary sites without bias driving. As such, a rapid V_{oc} decay would occur immediately the moment the illumination is removed. The V_{oc} decay rate was converted to the photoelectron lifetime (**Figure 8e**) according to the following equation [53-55]:

$$\tau = \frac{K_B T}{e} \left(\frac{dV_{oc}}{dt}\right)^{-1}$$

where τ is the potential-dependent photoelectron lifetime; K_B is the Boltzmann's constant; T is the temperature (300 K); e is the elementary charge; and V_{oc} is the open-circuit voltage [7,56]. We find that the photoelectrons of ZnO NFs can only exist at very high bias region, which indicates that the lack of fast pathways for photoelectron transporting to back contact and the restricted electron mobility at boundary defects of polycrystalline NFs can cause severe charge recombination in this system. Significantly, electron transport in nanoscale structures across microscale distances can be fulfilled through the secondary ZnO NW growth which constructs a well interconnected conduction network, the network enabling the photoelectron to transport along adjacent ZnO NWs back to substrate instead of traversing long distances along the axis of the ZnO NFs. The ~1.62 s photoelectron lifetime of the CZN-20 at +0.3 V versus RHE (**Table 1**), outperforming the ~0.66 s of CZN-10 and the ~0.73 s of CZN-15, certified that the CZN-20 has the best charge migration capability because of its increased junction area amongst long secondary branches. The ~25 nm ultrathin secondary NWs of the CZN-20 is more beneficial to the efficient charge separation and the minority carrier transfer to oxidation sites due to the shortened hole diffusion distance, which is in agreement with the J-V studies, and led to the highest photocurrent delivery. Compared to the reported PEC performance of currently studied pure ZnO nanostructures (**Table 2**), our "caterpillar-like" nanostructured network achieved one of the top PEC performance, not to mention our facile manufacturing capability and ease for production. Worth noting is that the vertically aligned nanoforests with controllable branch geometries recently reported by our group outperform the caterpillar-like nanostructures reported in this work in terms of PEC performances [30]. The maximum photocurrent density of the willow-like nanoforest photoanodes prepared by our group was only ~27% higher than the CZNs

at 1.2 V *vs.* Ag/AgCl while the synthesis procedure for the former is much more complicated, tedious and difficult to control. The seeding method to produce upstanding nanoforests confronts inevitable engineering obstacles notwithstanding it being considered as a main avenue to fabricate heterogeneous semiconductive nanostructures. The tentative attribution is that the willow-like nanoforest possesses a faster pathway for photocurrent transportation enabled by the vertical main trunks of the nanoforests, consistent with the fact that the photocurrent lifetime is longer in willow-like nanoforests than in CZNs. The longer photocurrent lifetime favors a lower probability of electron-hole recombination and leads to better PEC performance. However, it still will not stop the CZNs being one of the best models as ZnO nanostructures with no noble metal decoration and dopants embedded for efficient PEC water splitting applications. It is also expected that the PEC efficiency from this type of 3-D ZnO nanostructures would be further improved by nonmetallic and metallic doping and/or decoration by metallic NPs or QDs.

Discussions of **Figures 8c-e** also explain the discrepancy observed in **Figures 6c** and **8b**, which indicates that high $A + S = 100 - R - T$ does not necessarily guarantee high EC performance. The facilitated charge migration mechanism in the 3-D conduction networks and the shortened hole diffusion distance (L_D) of the optimum ZnO caterpillar photoanode, *i.e.* CZN-20, are illustrated in **Figure 8f**, and all aforementioned structural merits can greatly suppress the electron-hole recombination and be beneficial to the PEC performances. Although it is unlikely that a pure ZnO photoanode alone is capable of serving as a satisfactory PEC water splitting device owing to its wide band gap and low light corrosion resistance, the work demonstrated here provides a champion geometry with elucidated structure-property relationship and it can be in conjunction with nitrogen/hydrogen doping, sensitization, heterojunction and/or co-catalysts for engineering ideal PEC devices. Simultaneously, our simplified protocol and large-scale production may open a door to address the contradiction between the urgent needs of advanced PEC devices and devastating multi-step processing and micro-batch throughput of nanomaterials.

4. Conclusion

In conclusion, we demonstrate hierarchical “caterpillar-like” ZnO nanoarchitectures with highly dense nanowire branches originating from the seed-assembled ZnO nanofibers in a 360° fashion.

The networks composed of multilayered ZnO caterpillers present high-level spatial distribution of crystalline nanowires and hence build vital 3-D interconnected conduction pathways to improve the overall light-conversion efficiency. We implemented parametric investigations on light-geometry interactions to achieve champion caterpillar structure with ultralong and ultrathin branches for shortened minority carrier diffusion lengths. The photoelectrodes achieve a maximal photocurrent density of 0.72 $mA \cdot cm^{-2}$ at +1.2 V versus Ag/AgCl (0.209% conversion efficiency at +0.91 V versus RHE) under 1 sun illumination (100 $mW \cdot cm^{-2}$, AM 1.5G) without decorating with noble metal cocatalysts or quantum dot sensitizers. The protocol of constructing these 3-D caterpillar networks with high nanowire occupancy is substantially beneficial to hydrogen generation by means of (i) greatly increased light-harvesting/trapping capability enabled by boosted photoactive sites, long light penetration path and multi-reflections, (ii) improved electron migration to back contact due to interconnected conduction pathways confirmed by longer photoelectron lifetime, and (iii) optimum charge separation and hole transfer at the electrode/electrolyte interface on account of the ~25 nm ultrathin branches validated by electrochemical impedance spectroscopy study. Overall, our procedure to obtain the desirable CZN fetches in opportunities for facile and efficient fabrication of model photoelectrochemical anodes and would be applied to other materials for sustainable chemistry and engineering applications. A pure ZnO photoanode alone has its wide band gap and low light corrosion resistance, the demonstrated structures can be in conjunction with nitrogen/hydrogen doping, sensitization, heterojunction and/or co-catalysts for feasible industrial PEC applications.

Acknowledgements

The authors thank the support from the American Chemical Society – Petroleum Research Fund #51497 (YM), USDA National Institute of Food and Agriculture, HSI Collaboration: Integrating Food Science/Engineering and Education Network (IFSEEN, award number: 2015-38422-24059), and the National Science Foundation under DMR grant #1523577 (PREM: UTRGV-UMN Partnership for Fostering Innovation by Bridging Excellence in Research and Student Success).

References

[1] M. Gratzel, Photoelectrochemical Cells, Nature 414 (2001) 338-344.
[2] N. S. Lewis, Toward Cost-effective Solar Energy Use, Science 315 (2007) 798-801.
[3] J. A. Turner, A Realizable Renewable Energy Future, Science 285 (1999) 687-689.
[4] S. U. M. Khan, M. Al-Shahry, W. B. Ingler, Efficient Photochemical Water Splitting by a Chemically Modified n-TiO_2, Science 297 (2002) 2243-2245.
[5] A. Vojvodic, J. K. Norskov, Optimizing Perovskites for the Water-Splitting Reaction, Science, 334 (2011) 1355-1356.
[6] A. Fujishima, K. Honda, Electrochemical Photolysis of Water at a Semiconductor Electrode, Nature 238 (1972) 37-38.
[7] M. G. Walter, E. L. Warren, J. R. McKone, S. W. Boettcher, Q. X. Mi, E. A. Santori, N. S. Lewis, Solar Water Splitting Cells, Chem. Rev. 110 (2010) 6446-6473.
[8] F. E. Osterloh, Inorganic Nanostructures for Photoelectrochemical and Photocatalytic Water Splitting, Chem. Soc. Rev. 42 (2013) 2294-2320.
[9] J. H. Yang, D. G. Wang, H. X. Han, C. Li, Roles of Cocatalysts in Photocatalysis and Photoelectrocatalysis, Accounts Chem. Res. 46 (2013)1900-1909.
[10] E. M. P. Steinmiller, K. S. Choi, Photochemical Deposition of Cobalt-based Oxygen Evolving Catalyst on a Semiconductor Photoanode for Solar Oxygen Production, Proceeding Natl. Acad. Sci. USA, 106 (2009) 20633-20636.
[11] H. Pan, N. Misra, S. H. Ko, C. P. Grigoropoulos, N. Miller, E. E. Haller, O. Dubon, Melt-mediated Coalescence of Solution-deposited ZnO Nanoparticles by Excimer Laser Annealing for Thin-film Transistor Fabrication, Appl. Phys. A, 94 (2009) 111-115.
[12] S. H. Ko, D. Lee, H. W. Kang, K. H. Nam, J. Y. Yeo, S. J. Hong, C. P. Grigoropoulos, H. J. Sung, Nanoforest of Hydrothermally Grown Hierarchical ZnO Nanowires for a High Efficiency Dye-Sensitized Solar Cell, Nano Lett. 11 (2011) 666-671.
[13] Q. F. Zhang, C. S. Dandeneau, X. Y. Zhou, G. Z. Cao, ZnO Nanostructures for Dye-Sensitized Solar Cells, Adv. Mater. 21 (2009) 4087-4108.
[14] M. N. Huda, M. M. Al-Jassim, and J. A. Turner, Mott insulators: An Early Selection Criterion for Materials for Photoelectrochemical H_2 Production, J. Renew. Sustain. Ener. 3 [2011] 0531011-05310110.
[15] D. I. Suh, S. Y. Lee, T. H. Kim, J. M. Chun, E. K. Suh, O. B. Yang, S. K. Lee, The Fabrication and Characterization of Dye-sensitized Solar Cells with a Branched Structure of ZnO Nanowires, Chem. Phys. Lett. 442 [2007] 348-353.
[16] I. S. Cho, Z. B. Chen, A. J. Forman, D. R. Kim, P. M. Rao, T. F. Jaramillo, X. L. Zheng, Branched TiO_2 Nanorods for Photoelectrochemical Hydrogen Production, Nano Lett. 11 [2011] 4978-4984.
[17] Y. Mao, Branched Nanostructures for Photoelectrochemical Water Splitting, Nanomaterials and Energy 3 (2014) 103-128.
[18] A. Wolcott, W. A. Smith, T. R. Kuykendall, Y. P. Zhao, J. Z. Zhang, Photoelectrochemical Study of Nanostructured ZnO Thin Films for Hydrogen Generation from Water Splitting, Adv. Funct. Mater. 19 (2009) 1849-1856.
[19] C. Liu, X. B. Xu, A. J. E. Rettie, C. B. Mullins, D. L. Fan, One-step waferscale synthesis of 3-D ZnO Nanosuperstructures by Designed Catalysts for Substantial

Improvement of Solar Water Oxidation Efficiency, J. Mater. Chem. A, 1 (2013) 8111-8117.
[20] X. Y. Yang, A. Wolcott, G. M. Wang, A. Sobo, R. C. Fitzmorris, F. Qian, J. Z. Zhang, Y. Li, Nitrogen-Doped ZnO Nanowire Arrays for Photoelectrochemical Water Splitting, Nano Lett. 9 (2009) 2331-2336.
[21] M. Zhong, Y. Sato, M. Kurniawan, A. Apostoluk, B. Masenelli, E. Maeda, Y. Ikuhara, J. J. Delaunay, ZnO Dense Nanowire Array on a Film Structure in a Single Crystal Domain Texture for Optical and Photoelectrochemical Applications, Nanotechnology, 23 (2012) 495602.
[22] X. H. Lu, G. M. Wang, S. L. Xie, J. Y. Shi, W. Li, Y. X. Tong, Y. Li, Efficient Photocatalytic Hydrogen Evolution over Hydrogenated ZnO Nanorod Arrays, Chem. Commun. 48 (2012) 7717-7719.
[23] Y. F. Wei, L. Ke, J. H. Kong, H. Liu, Z. H. Jiao, X. H. Lu, H. J. Du, X. W. Sun, Enhanced Photoelectrochemical Water-splitting Effect with a Bent ZnO Nanorod Photoanode Decorated with Ag Nanoparticles, Nanotechnology, 23 (2012) 235401.
[24] W. Q. Wu, B. X. Lei, H. S. Rao, Y. F. Xu, Y. F. Wang, C. Y. Su, D. B. Kuang, Hydrothermal Fabrication of Hierarchically Anatase TiO_2 Nanowire Arrays on FTO Glass for Dye-sensitized Solar Cells, Sci. Rep. 3 (2013) 1352.
[25] J. Shi, Y. Hara, C. L. Sun, M. A. Anderson, X. D. Wang, Three-Dimensional High-Density Hierarchical Nanowire Architecture for High-Performance Photoelectrochemical Electrodes, Nano Lett. 11 (2011) 3413-3419.
[26] J. Y. Zheng, M. J. Kang, G. Song, S. I. Son, S. P. Suh, C. W. Kim, Y. S. Kang, Morphology Evolution of Dendritic Fe Wire Array by Electrodeposition, and Photoelectrochemical Properties of Alpha-Fe_2O_3 Dendritic Wire Array, Crystengcomm. 14 (2012) 6957-6961.
[27] R. Ghosh, M. K. Brennaman, T. Uher, M. R. Ok, E. T. Samulski, L. E. McNeil, T. J. Meyer, R. Lopez, Nanoforest Nb_2O_5 Photoanodes for Dye-Sensitized Solar Cells by Pulsed Laser Deposition, ACS Appl. Mater. Inter. 3 (2011) 3929-3935.
[28] X. Sun, Q. Li, Y. Lu, Y. Mao, Three-dimensional ZnO@MnO_2 Core@shell Nanostructures for Electrochemical Energy Storage, Chem. Commun. 49 (2013) 4456-8.
[29] Y. C. Qiu, K. Y. Yan, H. Deng, S. H. Yang, Secondary Branching and Nitrogen Doping of ZnO Nanotetrapods: Building a Highly Active Network for Photoelectrochemical Water Splitting, Nano Lett. 12 (2012) 407-413.
[30] X. Sun, Q. Li, J. C. Jiang, Y. Mao, Morphology-tunable Synthesis of ZnO Nanoforest and its Photoelectrochemical Performance, Nanoscale 6 (2014) 8769-8780.
[31] D. Lee, Y. Rho, F. I. Allen, A. M. Minor, S. H. Ko, C. P. Grigoropoulos, Synthesis of Hierarchical TiO_2 Nanowires with Densely-packed and Omnidirectional Branches, Nanoscale 5 (2013) 11147-11152.
[32] A. Kargar, K. Sun, Y. Jing, C. M. Choi, H. S. Jeong, Y. C. Zhou, K. Madsen, P. Naughton, S. H. Jin, G. Y. Jung, D. L. Wang, Tailoring n-ZnO/p-Si Branched Nanowire Heterostructures for Selective Photoelectrochemical Water Oxidation or Reduction, Nano Lett. 13 (2013) 3017-3022.
[33] K. A. Dick, K. Deppert, M. W. Larsson, T. Martensson, W. Seifert, L. R. Wallenberg, L. Samuelson, Synthesis of Branched 'Nanotrees' by Controlled Seeding of Multiple Branching Events, Nature Materials 3 (2004) 380-384.

[34] K. A. Dick, K. Deppert, T. Martensson, W. Seifert, L. Samuelson, Growth of GaP Nanotree Structures by Sequential Seeding of 1D Nanowires, J. Cryst. Growth 272 (2004) 131-137.
[35] K. Polychronopoulou, S. M. Aouadi, B. Sirota, D. S. Stone, L. Wang, P. Kohli, M. E. McCarroll, Hierarchical structures produced using unbalanced magnetron sputtering for photocatalytic degradation of Rhodamine 6G dye, J. Nanopart. Res. 16 (2013) 2180.
[36] H. Q. Yan, R. R. He, J. Johnson, M. Law, R. J. Saykally, P. D. Yang, Dendritic nanowire ultraviolet laser array, Journal of the American Chemical Society 125 (2003) 4728-4729.
[37] Q. Li, X. Sun, K. Lozano, Y. Mao, Facile and Scalable Synthesis of "Caterpillar-like" ZnO Nanostructures with Enhanced Photoelectrochemical Water-Splitting Effect, J. Phys. Chem. C, 118 (2014) 13467-13475.
[38] K. Sarkar, C. Gomez, S. Zambrano, M. Ramirez, E. de Hoyos, H. Vasquez, K. Lozano, Electrospinning to Forcespinning (TM), Mater. Today 13 (2010) 12-14.
[39] Y. Q. Dai, W. Y. Liu, E. Formo, Y. M. Sun, Y. N. Xia, Ceramic Nanofibers Fabricated by Electrospinning and Their Applications in Catalysis, Environmental Science, and Energy Technology, Polym. Advan. Technol. 22 (2011) 326-338.
[40] A. Altecor, Q. Li, K. Lozano, Y. Mao, Mixed-valent VO_x/polymer Nanohybrid Fibers for Flexible Energy Storage Materials, Ceramics International 40 (2014) 5073-5077.
[41] C. Jolley, V. Pool, Y. Idzerda, T. Douglas, All in the Packaging: Structural and Electronic Effects of Nanoconfinement on Metal Oxide Nanoparticles, Chemistry of Materials 23 (2011) 3921-3929.
[42] M. McCune, W. Zhang, Y. L. Deng, High Efficiency Dye-Sensitized Solar Cells Based on Three-Dimensional Multilayered ZnO Nanowire Arrays with "Caterpillarlike" Structure, Nano Lett. 12 (2012) 3656-3662.
[43] D. K. Roh, W. S. Chi, H. Jeon, S. J. Kim, J. H. Kim, High Efficiency Solid-State Dye-Sensitized Solar Cells Assembled with Hierarchical Anatase Pine Tree- like TiO_2 Nanotubes, Adv. Funct. Mater. 24 (2014) 379-386.
[44] J. M. Stiegler, R. Tena-Zaera, O. Idigoras, A. Chuvilin, R. Hillenbrand, Correlative Infrared-electron Nanoscopy Reveals the Local Structure-conductivity Relationship in Zinc Oxide Nanowires, Nat. Commun. 3 (2012) 1131.
[45] C. Richter, C. A. Schmuttenmaer, Exciton-like Trap States Limit Electron Mobility in TiO_2 Nanotubes, Nat. Nanotechnol. 5 (2010) 769-772.
[46] M. Scepanovic, M. Grujic-Brojcin, K. Vojisavljevic, S. Bernik, T. Sreckovic, Raman Study of Structural Disorder in ZnO Nanopowders, J. Raman Spectrosc. 41 (2010) 914-921.
[47] S. Singamaneni, M. Gupta, R. S. Yang, M. M. Tomczak, R. R. Naik, Z. L. Wang, V. V. Tsukruk, Nondestructive in Situ Identification of Crystal Orientation of Anisotropic ZnO Nanostructures, ACS Nano 3 (2009) 2593-2600.
[48] K. M. McPeak, T. P. Le, N. G. Britton, Z. S. Nickolov, Y. A. Elabd, J. B. Baxter, Chemical Bath Deposition of ZnO Nanowires at Near-Neutral pH Conditions without Hexamethylenetetramine (HMTA): Understanding the Role of HMTA in ZnO Nanowire Growth, Langmuir 27 (2011) 3672-3677.
[49] S. Xu, Z. L. Wang, One-dimensional ZnO Nanostructures: Solution Growth and Functional Properties, Nano Res. 4 (2011) 1013-1098.

[50] Z. H. Wen, S. M. Cui, H. H. Pu, S. Mao, K. H. Yu, X. L. Feng, J. H. Chen, Metal Nitride/Graphene Nanohybrids: General Synthesis and Multifunctional Titanium Nitride/Graphene Electrocatalyst, Adv. Mater. 23 (2011) 5445-5450.
[51] T. J. Athauda, J. G. Neff, L. Sutherlin, U. Butt, R. R. Ozer, Systematic Study of the Structure-Property Relationships of Branched Hierarchical TiO_2/ZnO Nanostructures, ACS Appl. Mater. Inter. 4 (2012) 6916-6925.
[52] B. Klahr, S. Gimenez, F. Fabregat-Santiago, T. Hamann, J. Bisquert, Water Oxidation at Hematite Photoelectrodes: The Role of Surface States, Journal of the American Chemical Society 134 (2012) 4294-4302.
[53] M. Zhou, H. B. Wu, J. Bao, L. Liang, X. W. Lou, Y. Xie, Ordered Macroporous $BiVO_4$ Architectures with Controllable Dual Porosity for Efficient Solar Water Splitting, Angew. Chem. Int. Edit. 52 (2013) 8579-8583.
[54] A. Zaban, M. Greenshtein, J. Bisquert, Determination of the Electron Lifetime in Nanocrystalline Dye Solar Cells by Open-circuit Voltage Decay Measurements, ChemPhysChem 4 (2003) 859-864.
[55] A. B. F. Martinson, J. W. Elam, J. T. Hupp, M. J. Pellin, ZnO Nanotube Based Dye-sensitized Solar Cells, Nano Lett. 7 (2007) 2183-2187.
[56] Y. J. Lin, Y. Xu, M. T. Mayer, Z. I. Simpson, G. McMahon, S. Zhou, D. W. Wang, Growth of p-Type Hematite by Atomic Layer Deposition and Its Utilization for Improved Solar Water Splitting, Journal of the American Chemical Society 134 (2012) 5508-5511.
[57] K. S. Ahn, Y. Yan, S. Shet, K. Jones, T. Deutsch, J. Turner, M. Al-Jassim, ZnO Nanocoral Structures for Photoelectrochemical Cells, Appl. Phys. Lett. 93 (2008) 163117.
[58] H. N. Chen, Z. H. Wei, K. Y. Yan, Y. Bai, Z. L. Zhu, T. Zhang, S. H. Yang, Epitaxial Growth of ZnO Nanodisks with Large Exposed Polar Facets on Nanowire Arrays for Promoting Photoelectrochemical Water Splitting, Small 10 (2014) 4760-4769.
[59] Y. K. Hsu, Y. G. Lin, Y. C. Chen Polarity-dependent Photoelectrochemical Activity in ZnO Nanostructures for Solar Water Splitting, Electrochem. Commun. 13 (2011) 1383-1386.
[60] M. Wu, W. J. Chen, Y. H. Shen, F. Z. Huang, C. H. Li, S. K. Li, In Situ Growth of Matchlike ZnO/Au Plasmonic Heterostructure for Enhanced Photoelectrochemical Water Splitting, ACS Appl. Mater. Inter. 6 (2014) 15052-15060.
[61] D. Pradhan, S. K. Mohapatra, S. Tymen, M. Misra, K. T. Leung, Morphology-Controlled ZnO Nanomaterials for Enhanced Photoelectrochemical Performance, Mater. Express 1 (2011) 59-67.
[62] X. Zhang, Y. Liu, Z. H. Kang, 3D Branched ZnO Nanowire Arrays Decorated with Plasmonic Au Nanoparticles for High-Performance Photoelectrochemical Water Splitting, ACS Appl. Mater. Inter. 6 (2014) 4480-4489.

Scheme caption

Scheme 1. Schematic illustration of the growth process and photoanode preparation of the 3-D "caterpillar-like" ZnO networks: (a) as-forcespun PVP/$Zn(NO_3)_2$ precursor fibers; (b) polycrystalline seed-assembled ZnO NFs after calcination; (c) hydrothermal growth of secondary branches originating from the ZnO NFs as hydrothermal growth seeds; (d) ripened 3-D "caterpillar-like" ZnO nanostructures on ITO substrates.

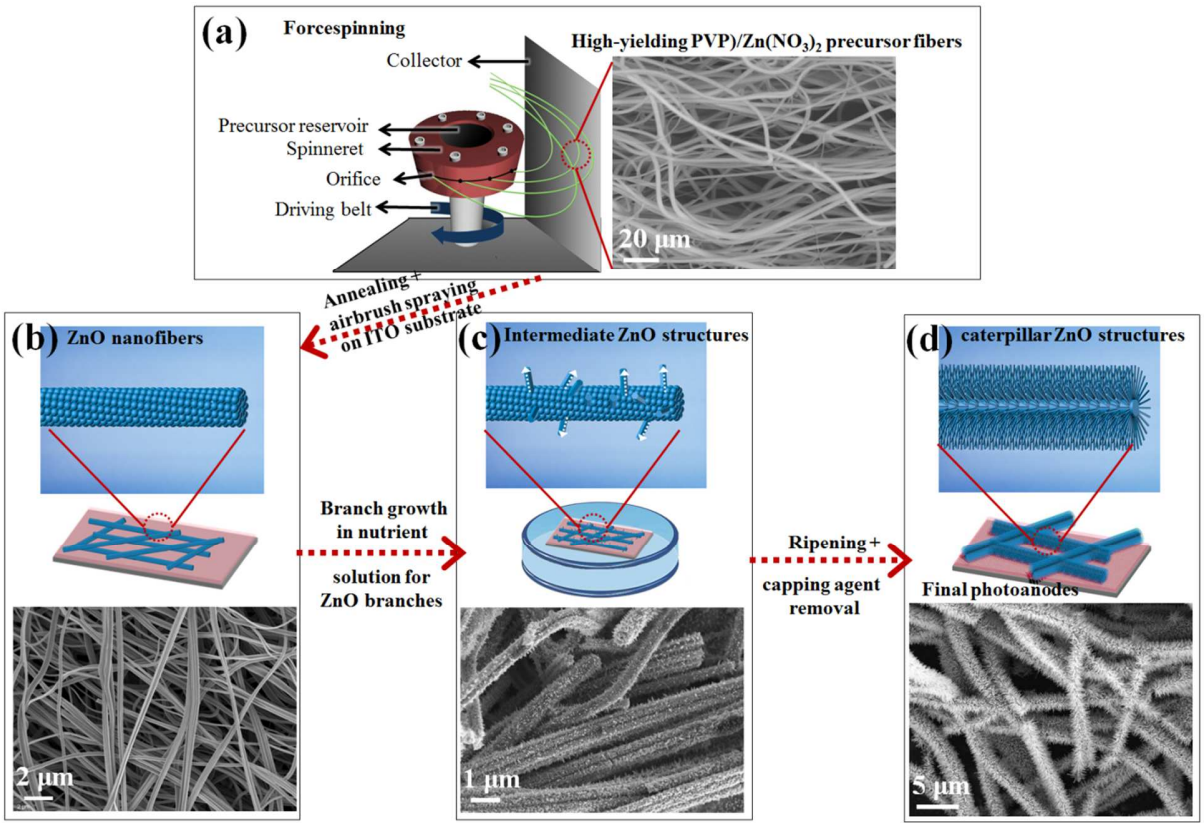

Scheme 1.

Figure captions

Figure 1. SEM images showing the growth process of the CZN-10: (a) parental ZnO NFs before secondary ZnO NW growth and after hydrothermal growth for (b) 1 h, (c) 2 h, (d) 3 h, (e) 4 h and (f) 5h.

Figure 2. Plan-view and cross-section SEM images of (a, b) CZN-10, (c, d) CZN-15, and (e, f) CZN-20. The insets of (b, d and f) represent corresponding high magnification SEM images.

Figure 3. CZN-10: (a) SEM image, (c) TEM image and SAED pattern of an individual caterpillar, and (e) HRTEM image of a single NW. CZN-20: (b) SEM image, (d) TEM image and SAED pattern of an individual caterpillar. (f) HRTEM image and SAED pattern of a single NW.

Figure 4. XRD patterns and Raman spectra of (a) ZnO NFs (b) CNZ-10, (c) CNZ-15 and (d) CNZ-20. The XRD experiments were performed on the ZnO NFs and CZNs supported by regular glass substrates to avoid the confusion caused by the overlapping of (400) peak of ITO and (0002) peak of ZnO.

Figure 5. Geometry factor plot of the ZnO branch length and diameter of various "caterpillar-like" ZnO nanostructures as a function of ammonia concentration. SEM images showing the structural evolution of the "caterpillar-like" ZnO nanostructures prepared in solutions with 0.025 M $Zn(NO_3)_2 \cdot 6H_2O$, 0.025 M HMTA, 0.0035 M PEI, and different $NH_3 \cdot H_2O$ concentrations: (a) $c(NH_3 \cdot H_2O)$ = 0 M, (b) $c(NH_3 \cdot H_2O)$ = 0.05 M, (c) $c(NH_3 \cdot H_2O)$ = 0.10 M, (d) $c(NH_3 \cdot H_2O)$ = 0.15 M, (e) $c(NH_3 \cdot H_2O)$ = 0.20 M, and (f) $c(NH_3 \cdot H_2O)$ = 0.25 M at 95°C for 5 h.

Figure 6. (a) Transmittance, (b) reflectance, and (c) absorption plus scattering spectra (it is worth noticing that $A + S = 100 - R - T$ instead of $A = 100 - T$ for highly rough topography to wit the loss of light transmission is mainly as a result of reflection and scattering) of the ZnO NFs and three representative CZNs. (d) Schematic illustration demonstrating the enhanced light-harvesting, the open structure and the scattering effect of the CZNs.

Figure 7. AFM images of the "caterpillar-like" ZnO nanostructures: (a) ZnO NFs, (b) CNZ-10, (c) CNZ-15 and (d) CNZ-20.

Figure 8. (a) J-V curves recorded at a scan rate of 10 mV s^{-1} under 1 sun illumination (100 mW cm^{-2} AM 1.5G), (b) Photoconversion efficiency (η) as a function of applied potential referenced to RHE. (c) EIS at a frenquency range of 1 M to 0.01 Hz with DC = 0.3 V, (d) responses of V_{oc} and (e) reckoned photoelectron lifetimes as a function of applied potential referenced to RHE of the "caterpillar-like" ZnO nanostructures. (f) Schematic illustration demonstrating shortened hole diffusion length and electron transport pathways, which benefit the exciton dissociation.

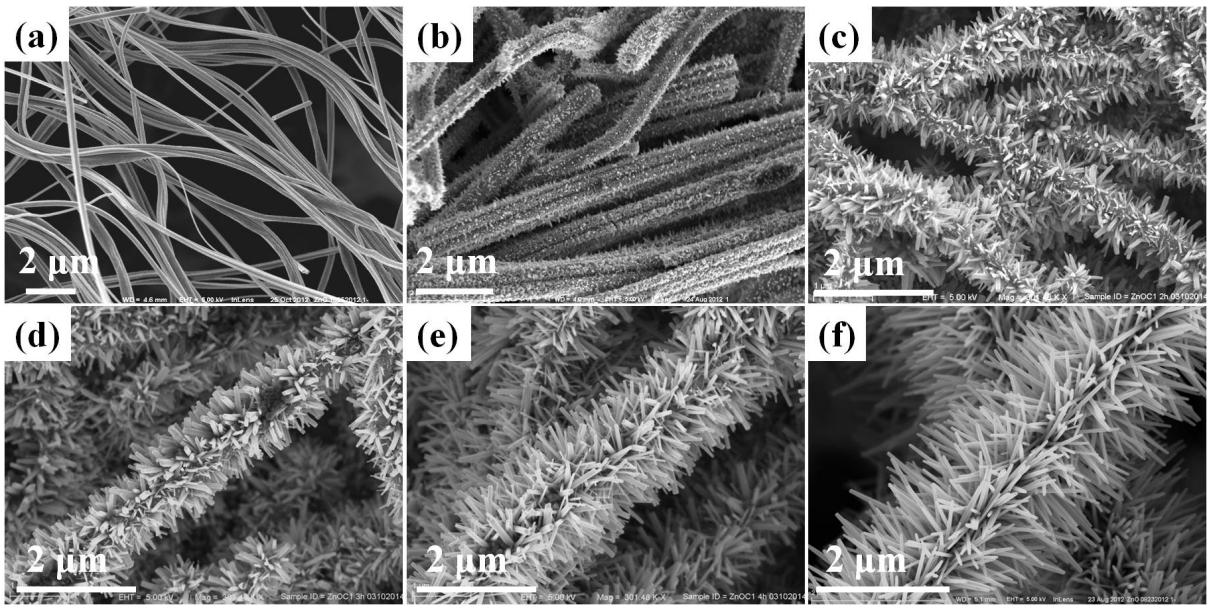

Figure 1.

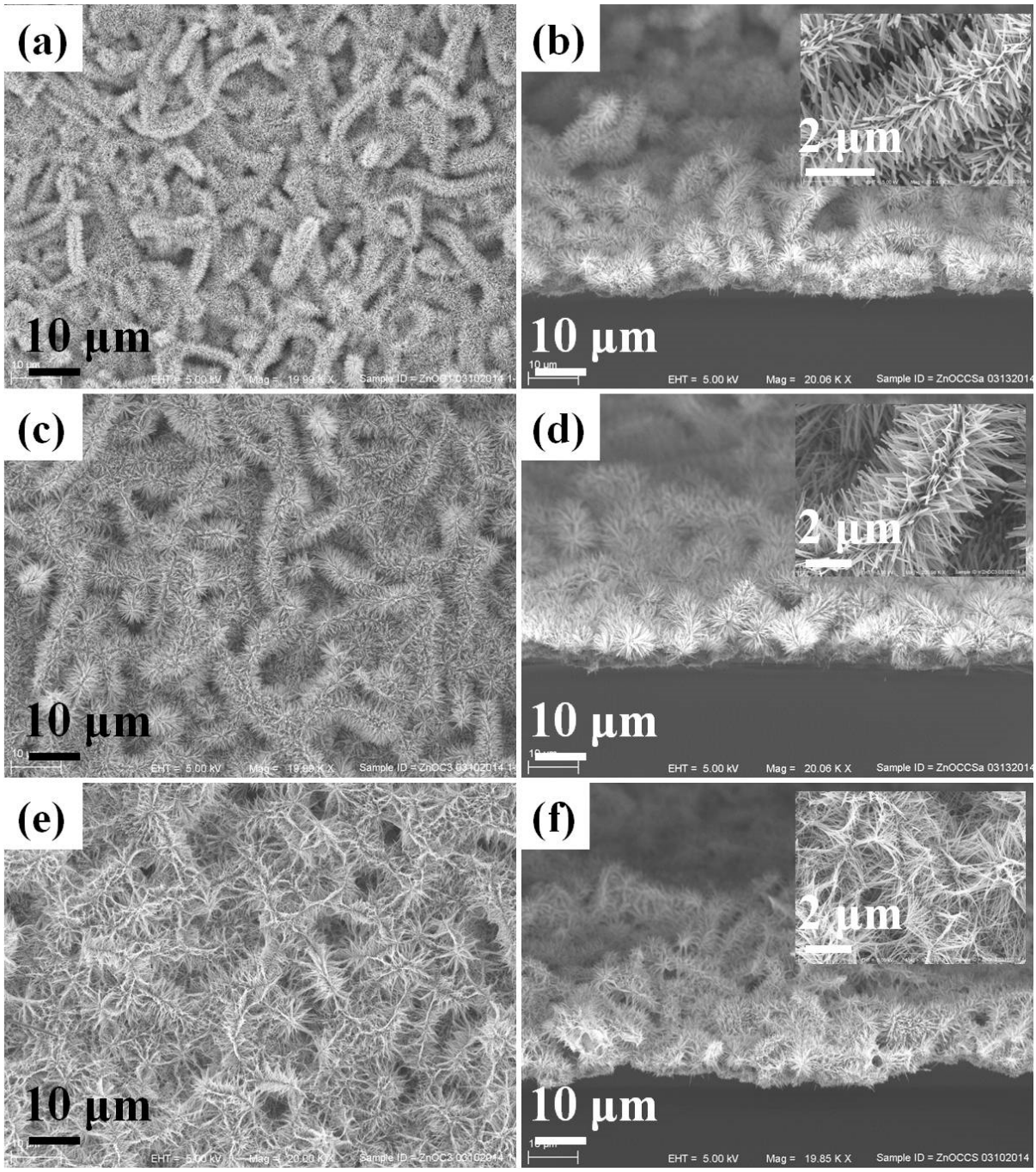
(a)
10 µm
(b)
2 µm
10 µm
EHT = 5.00 kV
Mag = 20.06 K X
Sample ID = ZnOCCSa 0313201
(c)
10 µm
(d)
2 µm
10 µm
EHT = 5.00 kV
Mag = 20.06 K X
Sample ID = ZnOCCSa 0313201
(e)
10 µm
(f)
2 µm
10 µm
EHT = 5.00 kV
Mag = 19.85 K X
Sample ID = ZnOCCS 03102014

Figure 2.

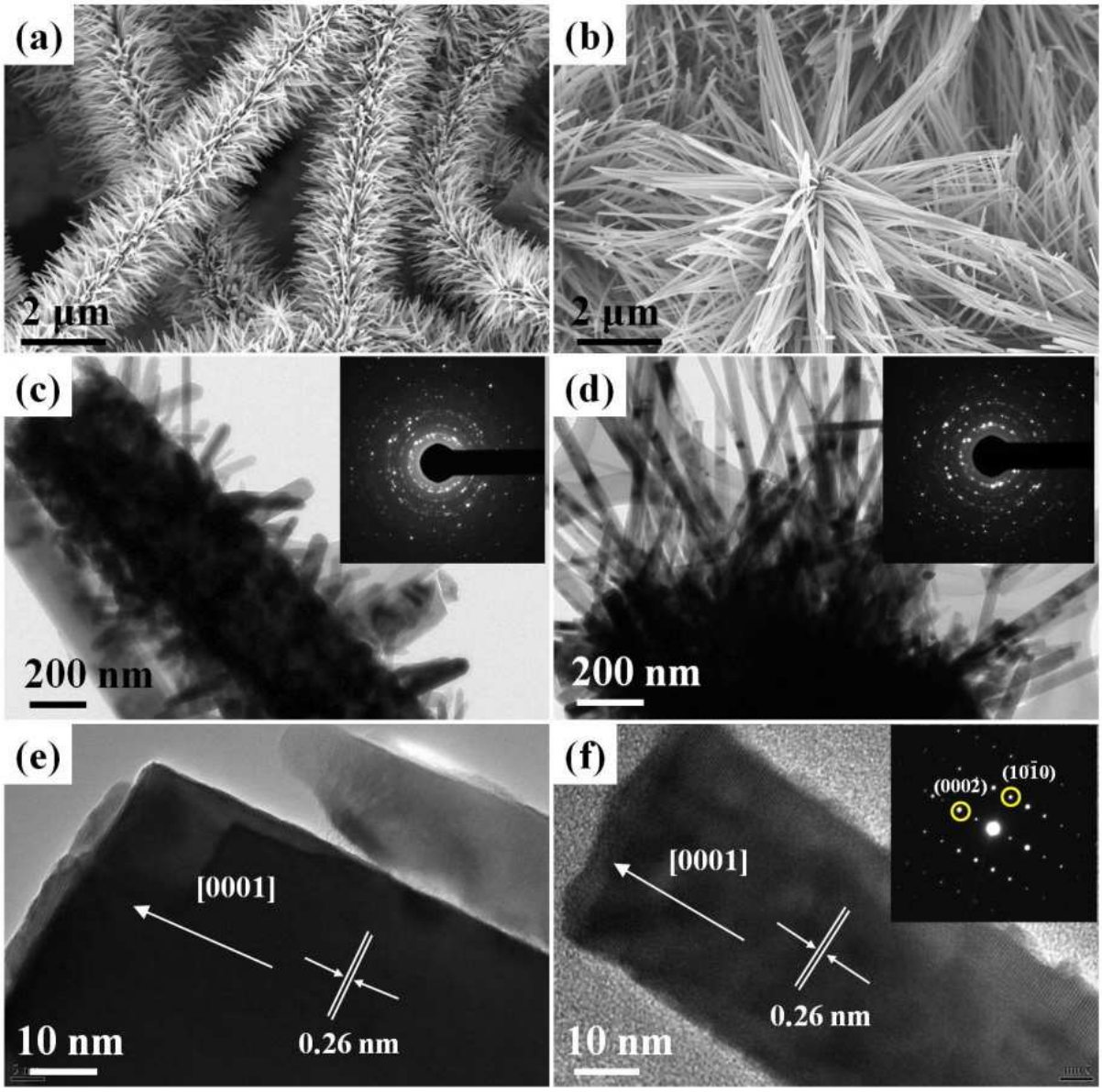
(a)
2 μm
(b)
2 μm
(c)
200 nm
(d)
200 nm
(e)
[0001]
0.26 nm
10 nm
(f)
(0002)
(10$\bar{1}$0)
[0001]
0.26 nm
10 nm

Figure 3.

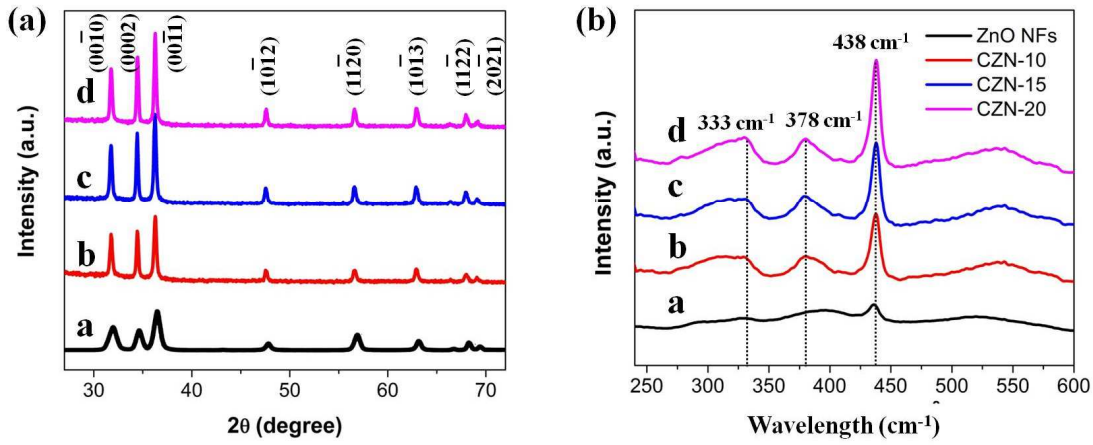

Figure 4.

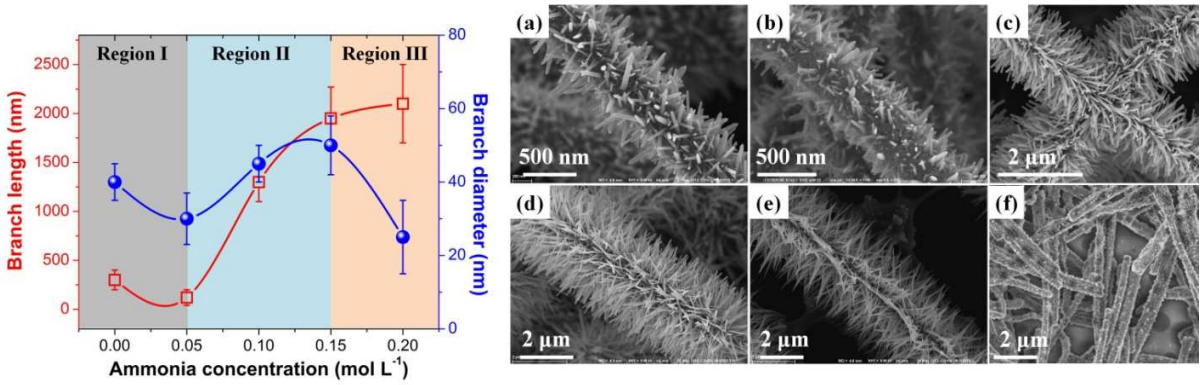

Figure 5.

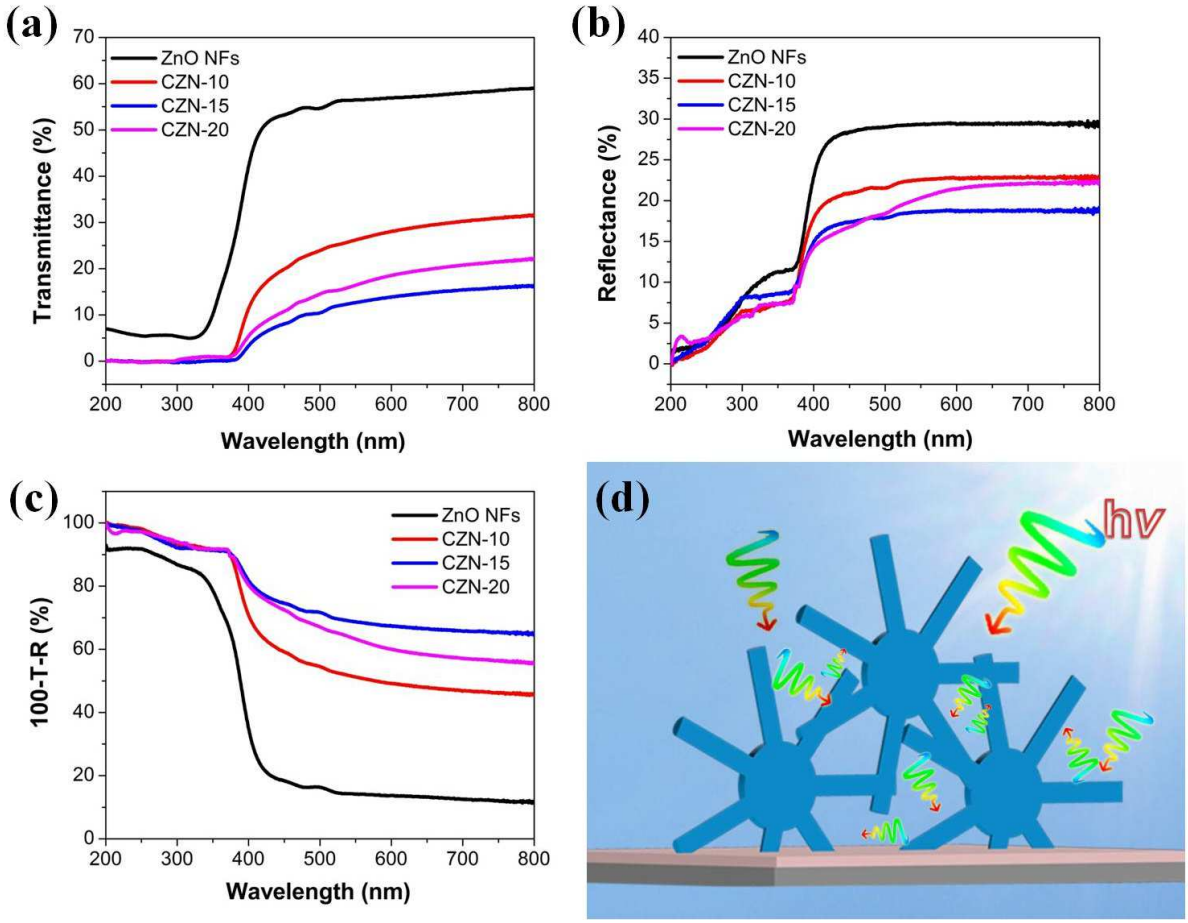
(a)
Transmittance (%)
Wavelength (nm)
ZnO NFs
CZN-10
CZN-15
CZN-20
(b)
Reflectance (%)
Wavelength (nm)
ZnO NFs
CZN-10
CZN-15
CZN-20
(c)
100-T-R (%)
Wavelength (nm)
ZnO NFs
CZN-10
CZN-15
CZN-20
(d)
hv

Figure 6.

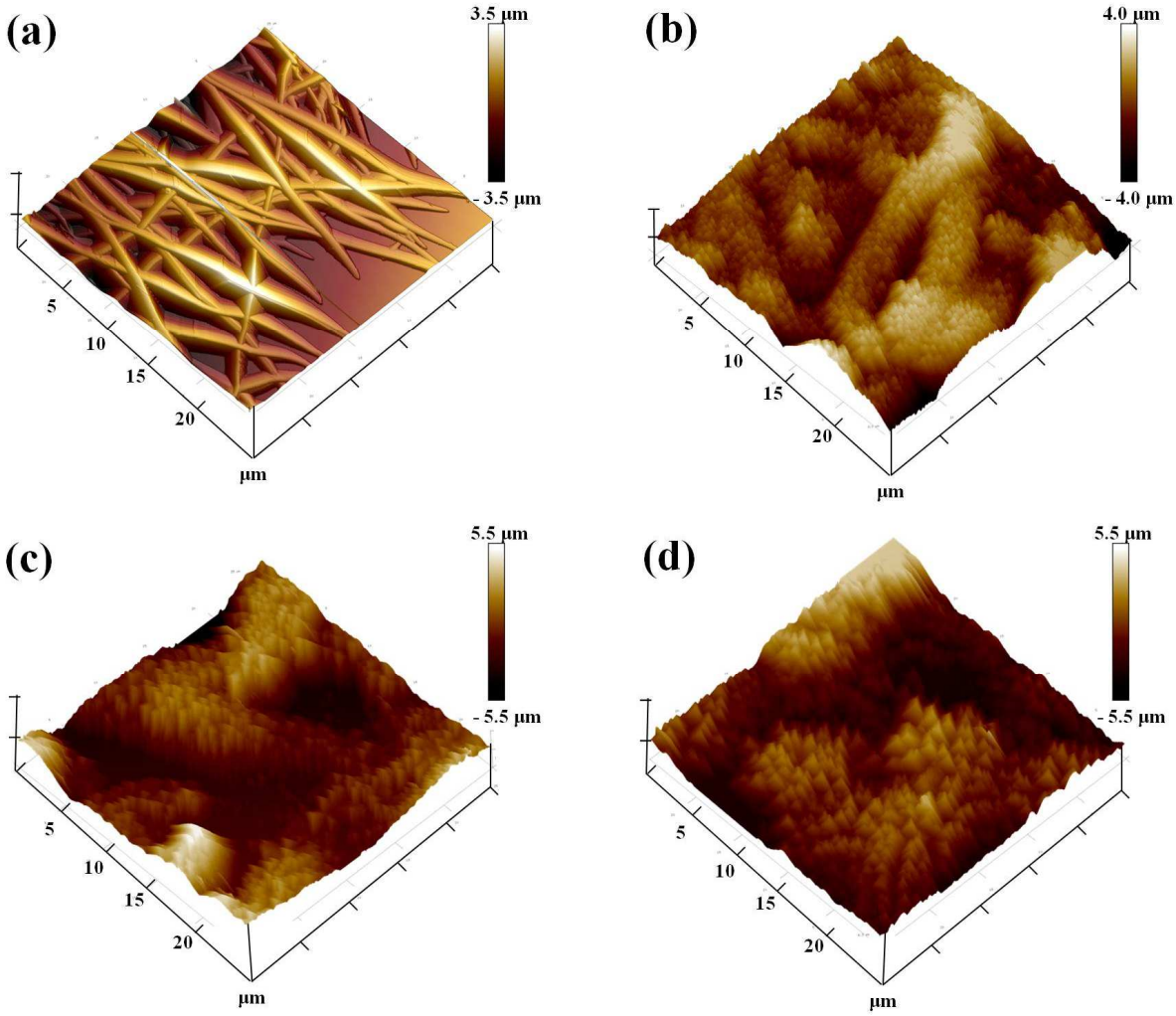
(a)
3.5 µm
- 3.5 µm
5
10
15
20
µm
(b)
4.0 µm
- 4.0 µm
5
10
15
20
µm
(c)
5.5 µm
- 5.5 µm
5
10
15
20
µm
(d)
5.5 µm
- 5.5 µm
5
10
15
20
µm

Figure 7.

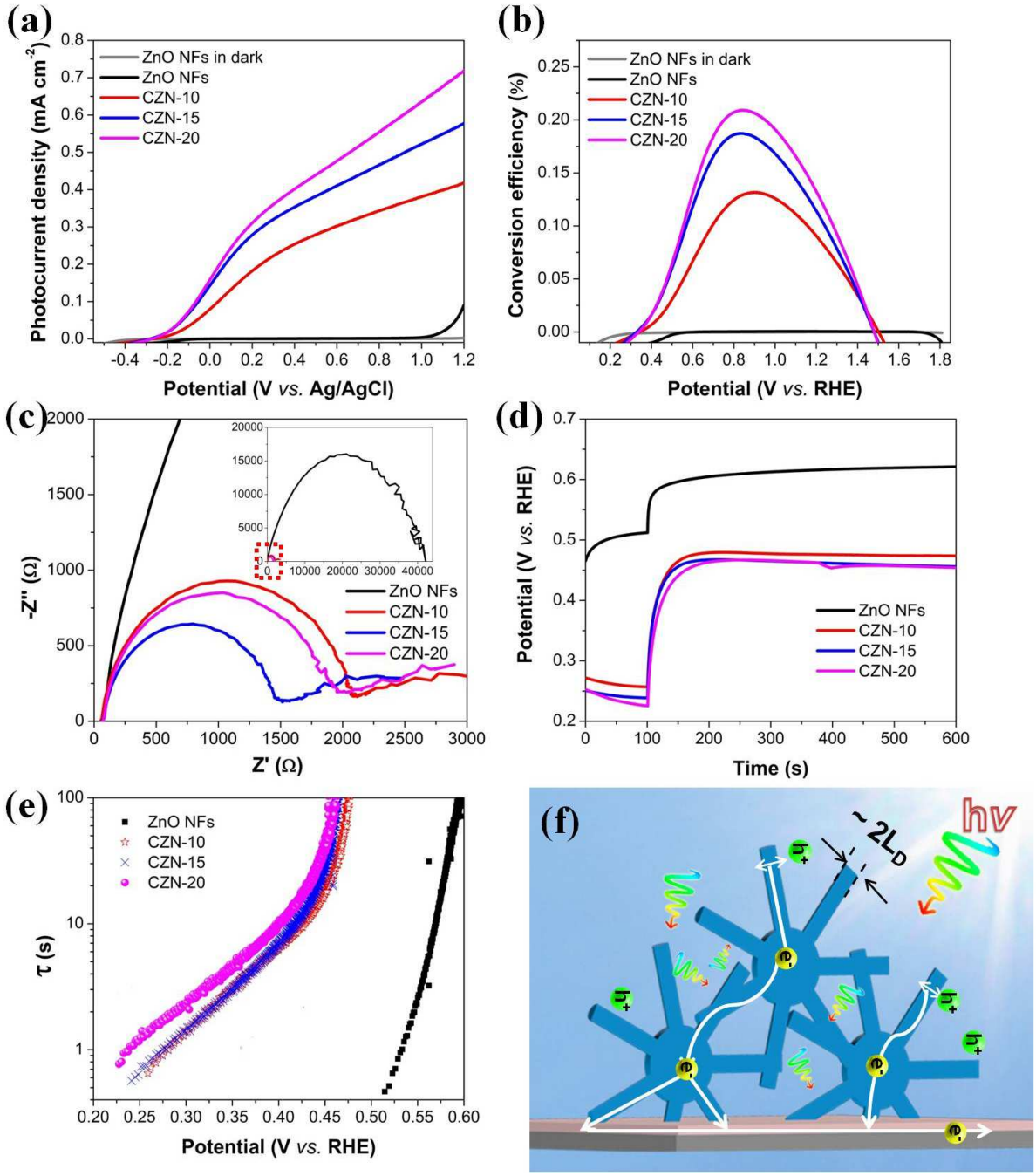
(a)
Photocurrent density (mA cm^{-2})
Potential (V vs. Ag/AgCl)
ZnO NFs in dark
ZnO NFs
CZN-10
CZN-15
CZN-20
(b)
Conversion efficiency (%)
Potential (V vs. RHE)
(c)
-Z'' (Ω)
Z' (Ω)
(d)
Potential (V vs. RHE)
Time (s)
(e)
τ (s)
Potential (V vs. RHE)
(f)
~ 2L$_D$
hv
e$^-$
h$^+$

Figure 8.

Table captions

Table 1. Summary of the geometric information and PEC performance of the synthesized ZnO NFs and CZNs.

Table 2. Comparison of reported undoped pure ZnO nanostructures with the current work as photoanodes for water splitting applications.

Table 1.

Sample	Branch length [nm]	Branch diameter [nm]	J @ 0.5 V [mA·cm^{-2}][a)]	J @ 1.2 V [mA·cm^{-2}][a)]	Efficiency [%]	R_{ct} [Ω]	R_a [nm]	V_{oc} [V][b)]	Photoelectron lifetime @0.3 V [s][b)]
ZnO NFs	-	-	0.0011	0.089	0.00066	42166.3	761.1	0.469	-
CZN-10	1300 ± 200	45 ± 5	0.28	0.41	0.132	2134.3	900.7	0.272	0.66
CZN-15	1950 ± 320	50 ± 8	0.38	0.58	0.187	1398.1	1292.0	0.251	0.73
CZN-20	2200 ± 400	25 ± 10	0.44	0.72	0.209	1969.8	1207.0	0.253	1.62

[a)] The potential is referenced to Ag/AgCl; [b)] The potential is referenced to RHE.

Table 2.

Materials	Morphological features	Electrolyte	Conditions	Performance	Ref.
ZnO (nanoparticles)[1]	15-40 nm particles, 500 nm thick film	0.5 M $NaClO_4$, pH = 7.4	I = 230 mW cm^{-2}, λ = 350–800 nm, 1000W Xe lamp	j = 0.142 mA cm^{-2} at 1.0 V *vs.* Ag/AgCl	[18]
ZnO (nanocoral)[2]	Nanocorals consisting of nanosheets	0.5 M $NaSO_4$, pH = 6.8	I = 125 mW cm^{-2}, λ = 350–750 nm, W-halogen lamp	j = 0.25 mA cm^{-2} at 1.2 V *vs.* RHE	[57]
ZnO (NWs/nanodisks)[3]	Nanodisks with 150-200 nm lateral diameter on NWs	0.5 M $NaSO_4$, pH = 6.5	I = 100 mW cm^{-2}, λ = 300–700 nm, 150 W Xe lamp	j = ~0.44 mA cm^{-2} at 1.2 V *vs.* Ag/AgCl, η_{max}=0.1%	[58]
ZnO (nanotetrapods)[4]	Nanotetrapods branched by 50-300 nm long NRs	0.5 M $NaSO_4$, pH = 7.0	I = 100 mW cm^{-2}, λ = 350–800 nm, AM 1.5 G	j = 0.12 mA cm^{-2} at 0.92 V *vs.* RHE, η_{max}=0.045%	[29]
ZnO (nanotubes & nanosheets)[5]	Hollow nanotubes & 2-D nanosheet arrays	0.5 M $NaSO_4$	I = 100 mW cm^{-2}, λ = 300–700 nm, 150 W Xe lamp	j = ~ 0.27 & 0.51 mA cm^{-2} at 1.0 V *vs.* Ag/AgCl	[59]
ZnO (NRs before Au coating)[6]	NRs with 4 um in length and 300-400 nm in diameter	0.1 M $NaSO_4$, pH = 7.0	I = 100 mW cm^{-2}, λ = 300–700 nm, 150 W Xe lamp	j = 0.33 mA cm^{-2} at 1.0 V *vs.* Ag/AgCl, η_{max}=0.03%	[60]
ZnO (nanowalls)[7]	50-200 nm thick nanowalls assembled by 20-30 nm nanograins, 20 um thick film	1 M KOH	I = 100 mW cm^{-2}, 300 W solar simulator	j = 0.54 (1.56 after doping) mA cm^{-2} at 0.5 V *vs.* Ag/AgCl	[61]
ZnO (branched NWs decorated without plasmonic Au NPs)[8]	NWs branched by 200 nm long NRs	0.5 M $NaSO_4$, pH = 7.0	I = 100 mW cm^{-2}, 300 W Xe lamp	j = 0.67 mA cm^{-2} at 1.0 V *vs.* Ag/AgCl, η_{max}=0.24%	[62]
ZnO (brush & willow-like nanoforest)[9]	Nanoforests with moderate and high aspect ratio branches	0.5 M $NaSO_4$, pH = 7.0	I = 100 mW cm^{-2}, λ = 350–800 nm, AM 1.5 G solar simulator	j = 0.73 & 0.92 mA cm^{-2} at 1.2 V *vs.* Ag/AgCl, η_{max}=0.236 & 0.299%	[30] (our group)
CZN-10 (caterpillars)	Branches with 1.3 um in length and 45 nm in diameter that derive from NFs	0.5 M $NaSO_4$, pH = 7.0	I = 100 mW cm^{-2}, λ = 350–800 nm, AM 1.5 G solar simulator	j = 0.41 mA cm^{-2} at 1.2 V *vs.* Ag/AgCl, η_{max}=0.132%	This work
CZN-15 (caterpillars)	Branches with 1.95 um in length and 50 nm in diameter that derive from NFs	0.5 M $NaSO_4$, pH = 7.0	I = 100 mW cm^{-2}, λ = 350–800 nm, AM 1.5 G solar simulator	j = 0.58 mA cm^{-2} at 1.2 V *vs.* Ag/AgCl, η_{max}=0.187%	This work
CZN-20 (caterpillars)	Branches with 2.2 um in length and 25 nm in diameter that derive from NFs	0.5 M $NaSO_4$, pH = 7.0	I = 100 mW cm^{-2}, λ = 350–800 nm, AM 1.5 G solar simulator	j = 0.72 mA cm^{-2} at 1.2 V *vs.* Ag/AgCl, η_{max}=0.209%	This work

Notes: NWs, NRs and NFs denote nanowires, nanorods and nanofibers, respectively.